Bispecific antibody neutralizes circulating SARS-CoV-2 variants, prevents escape and protects mice from disease

Raoul De Gasparo[a,#], Mattia Pedotti[a,#], Luca Simonelli[a], Petr Nickl[b], Frauke Muecksch[h], Irene Cassaniti [k], Elena Percivalle[k], Julio C. C. Lorenzi[i], Federica Mazzola[a], Davide Magrì[j], Tereza Michalcikova[b], Jan Haviernik[c], Vaclav Honig[c,d], Blanka Mrazkova[b], Natalie Polakova[b], Andrea Fortova[c], Jolana Tureckova[b], Veronika Iatsiuk[b], Salvatore Di Girolamo[a], Martin Palus[c,d], Dagmar Zudova[b], Petr Bednar[c,e], Ivana Bukova[b], Filippo Bianchini[a], Dora Mehn[j], Radim Nencka[f], Petra Strakova[c], Oto Pavlis[g], Jan Rozman[b], Sabrina Gioria[j], Josè Camilla Sammartino[k], Federica Giardina[k], Stefano Gaiarsa[k], Qiang Pan Hammarström[m], Christopher O. Barnes[n], Pamela J. Bjorkman[n], Luigi Calzolai[j], Antonio Piralla[k], Fausto Baldanti[k], Michel C. Nussenzweig[i,l], Paul D. Bieniasz[h,l], Theodora Hatziioannou[h], Jan Prochazka[b], Radislav Sedlacek[b], Davide F. Robbiani[a*], Daniel Ruzek[c,d*], Luca Varani[a*].

[a] Institute for Research in Biomedicine, Università della Svizzera italiana (USI), Bellinzona, Switzerland
[b] Czech Centre of Phenogenomics, Institute of Molecular Genetics of the Czech Academy of Sciences, Vestec, Czech Republic.
[c] Veterinary Research Institute, Brno, Czech Republic
[d] Institute of Parasitology, Biology Centre of the Czech Academy of Sciences, Ceske Budejovice, Czech Republic
[e] Faculty of Science, University of South Bohemia, Ceske Budejovice, Czech Republic
[f] Institute of Organic Chemistry and Biochemistry of the Czech Academy of Sciences, Prague, Czech Republic
[g] Center of Biological Defense, Military Health Institute, Military Medical Agency, Techonin, Czech Republic
[h] Laboratory of Retrovirology, The Rockefeller University, New York, NY, USA
[i] Laboratory of Molecular Immunology, The Rockefeller University, New York, NY, USA
[j] European Commission, Joint Research Centre, Ispra, VA, Italy
[k] Molecular Virology Unit, Microbiology and Virology Department, Fondazione IRCCS Policlinico San Matteo, Pavia, Italy
[l] Howard Hughes Medical Institute, The Rockefeller University, New York, NY, USA
[m] Department of Biosciences and Nutrition, Karolinska Institutet, SE14183, Huddinge, Sweden
[n] Division of Biology and Biological Engineering, California Institute of Technology, Pasadena, CA, USA

[#] These authors contributed equally
[*] Corresponding authors

Summary

Neutralizing antibodies targeting the receptor binding domain (RBD) of the SARS-CoV-2 Spike (S) are among the most promising approaches against coronavirus disease 2019 (COVID-19)[1,2]. We developed a bispecific, IgG1-like molecule (CoV-X2) based on two antibodies derived from COVID-19 convalescent donors, C121 and C135[3]. CoV-X2 simultaneously binds two independent sites on the RBD and, unlike its parental antibodies, prevents detectable S binding to Angiotensin-Converting Enzyme 2 (ACE2), the virus cellular receptor. Furthermore, CoV-X2 neutralizes SARS-CoV-2 and its variants of concern, as well as the escape mutants generated by the parental monoclonals. In a novel animal model of SARS-CoV-2 infection with lung inflammation, CoV-X2 protects mice from disease and suppresses viral escape. Thus, simultaneous targeting of non-overlapping RBD epitopes by IgG-like bispecific antibodies is feasible and effective, combining into a single molecule the advantages of antibody cocktails.

54   The COVID-19 pandemic prompted an unprecedented effort to develop effective countermeasures

55   against SARS-CoV-2. Pre-clinical data and phase III clinical studies indicate that monoclonal

56   antibodies (mAbs) could be effectively deployed for prevention or treatment during the viral

57   symptoms phase of the disease[1,2]. Cocktails of two or more mAbs are preferred over a single

58   antibody for increased efficacy and prevention of viral escape. However, this approach requires

59   increased manufacturing costs and volumes, which are problematic at a time when the supply chain

60   is under pressure to meet the high demand for COVID-19 therapeutics, vaccines and biologics in

61   general[4]. Cocktails also complicate formulation[5,6] and hinder novel strategies like antibody

62   delivery by viral vectors or by non-vectored nucleic acids[7-9]. Instead, multispecific antibodies

63   embody the advantages of a cocktail within a single molecule.

64   To this avail, we employed structural information[10] and computational simulations to

65   design bispecifics that would simultaneously bind to (i) independent sites on the same RBD and

66   (ii) distinct RBDs on a S trimer. Out of several designs evaluated by atomistic Molecular Dynamics

67   simulations, 4 were produced and CoV-X2 was the most potent neutralizer of SARS-CoV-2

68   pseudovirus, with half-maximal inhibitory concentration (IC_{50}) = 0.04 nM (5.8 ng/mL) (Extended

69   Data Fig.1). CoV-X2 is a human-derived, CrossMAb-format IgG1-like bispecific antibody[11]

70   resulting from the combination of the Fragment antigen binding (Fab) of mAbs C121 and C135,

71   two potent SARS-CoV-2 neutralizers[3]. Structural predictions showed that CoV-X2, but not its

72   parental monoclonals, can bind bivalently to all RBD conformations on the S trimer, preventing

73   ACE2 access (Fig.1a and Extended Data Fig.2)[12].

74   CoV-X2 bound with low nanomolar affinity to RBD, S trimer, and to several mutants,

75   including the naturally occurring variants B.1 (D614G in S protein), B.1.1.7 (N501Y in RBD) and

76   B.1.351 (K417N, E484K and N501Y in RBD)[13,14], and the escape mutants of the parental mAbs[15]

77   (Extended Data Figs.3-5).
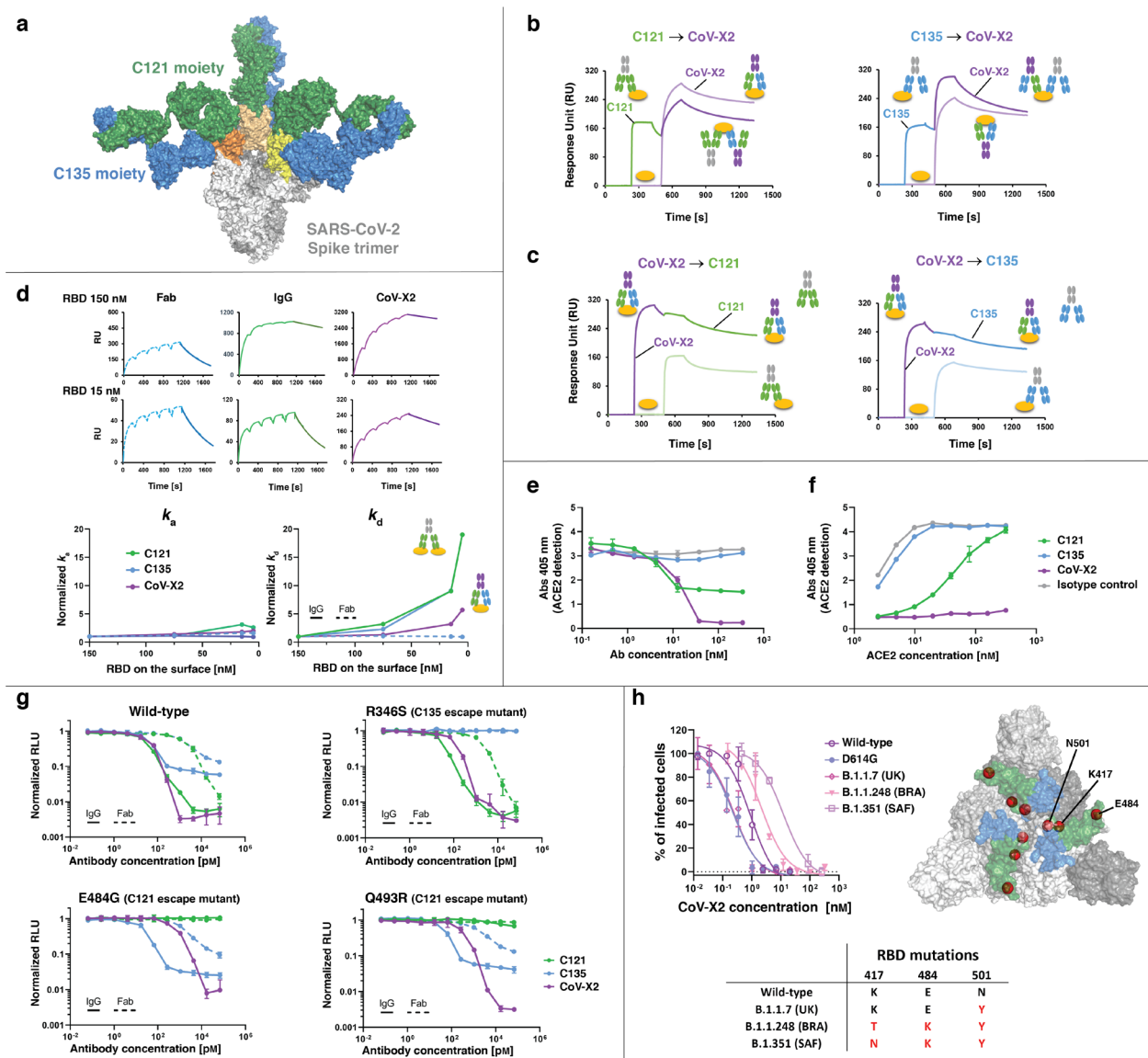
78
79   **Fig.1 | Biochemical and *in vitro* neutralizing properties of CoV-X2 are superior to its parental mAbs.**
80   **a,** Computational simulations predict bivalent binding of CoV-X2 to all three RBDs on the S trimer (see
81   also Extended Data Fig.2). Green and blue are C121 and C135 moieties, respectively; RBDs are in shades
82   of yellow/orange. **b, c,** SPR demonstrates that both arms of CoV-X2 are functional. In (**b**), immobilized
83   RBD complexed with the indicated mAb (first antibody) binds to CoV-X2 (second antibody). In (**c**), the
84   RBD/CoV-X2 complex prevents binding by the single mAbs. Shaded colors are controls (second antibody
85   only). **d,** Both arms of CoV-X2 bind simultaneously to the RBD since, contrary to the monoclonals, avidity
86   is retained at decreasing RBD concentrations. On top, representative SPR traces indicating the different
87   dissociations of antibodies (or Fab) binding to RBD immobilized at different concentrations on the SPR
88   chip (see also Extended Data Fig.6). At the bottom, plots of the normalized k_a and k_d values obtained with
89   different concentrations of immobilized RBD. Increasing normalized dissociation rate (k_d) values indicate
90   loss of avidity. **e, f,** CoV-X2 fully prevents ACE2 binding to S trimer in ELISA. ACE2 binding to

91   antibody/S trimer complexes is measured either with increasing concentration of the indicated antibody and
92   constant ACE2 (**e**), or at constant antibody concentration with increasing ACE2 (**f**). Mean with standard
93   deviation of two experiments is shown. **g,** CoV-X2 neutralizes SARS-CoV-2 pseudovirus and escape
94   mutants of its parental mAbs. Normalized relative luminescence (RLU) for cell lysates after infection with
95   nanoluc-expressing SARS-CoV-2 pseudovirus in the presence of increasing concentrations of antibodies.
96   Wild-type SARS-CoV-2 pseudovirus (left) is shown alongside three escape mutants generated in the
97   presence of C121 or C135[15]. Dashed lines are parental Fabs. Mean with standard deviation; one of two
98   independent experiments. **h,** Neutralization of SARS-CoV-2 isolates with sequences corresponding to
99   viruses first isolated in China (wild-type), Italy (D614G), United Kingdom (UK; B.1.1.7), Brazil (BRA;
100   B.1.1.248) and South Africa (SAF; B.1.351). RBD residues mutated in the variants are indicated in the
101   table and as red spheres on the S trimer structure, where the epitope of C135 (blue) and C121 (green) are
102   shown.
103
104
105   CoV-X2 also bound to pre-formed C121/RBD and C135/RBD complexes, thus confirming

106   that both of its arms are functional (Fig.1b,c). Next, an avidity assay by Surface Plasmon

107   Resonance (SPR) was used to experimentally confirm the computational prediction that CoV-X2

108   can simultaneously engage two sites on the same RBD (Methods, Fig.1d and Extended Data Fig.6).

109   Avidity occurs when IgGs bind bivalently to antigens, resulting in slower dissociation rates (k_d)

110   (Extended Data Fig.6a). Accordingly, C121 and C135 IgG showed avidity at high antigen

111   concentrations due to inter-molecular binding of adjacent RBDs; at lower antigen concentrations

112   the dissociation rate was instead faster since inter-molecular binding was prevented by the

113   increased distance between RBD molecules, resulting in loss of avidity. Intra-molecular avidity is

114   not possible for C121 and C135 since a single epitope is available on each RBD molecule. By

115   contrast, CoV-X2 maintained avidity even at low antigen concentrations, indicating bivalent, intra-

116   molecular binding (Fig.1d and Extended Data Fig.6). ELISA assays were then performed to

117   evaluate the ability of CoV-X2 to inhibit the binding of recombinant ACE2 to the S trimer

118   (Fig.1e,f). In line with the structural information[10], C135 did not affect the ACE2/S interaction.

119   C121, which occupies the ACE2 binding site on the RBD, prevented ACE2 binding but only

120   partially. By contrast, ACE2 binding was not detected in the presence of CoV-X2, suggesting a

121   synergistic effect by the two moieties composing the bispecific.

122   To assess the neutralizing ability of CoV-X2 *in vitro*, we first used SARS-CoV-2

123   pseudoviruses[16]. The bispecific neutralized pseudovirus carrying wild-type SARS-CoV-2 S at sub-

124   nanomolar concentrations (IC_{50} = 0.04 nM (5.8 ng/mL); IC_{90} = 0.3 nM (44 ng/mL)), which was

125   similar or better than the parental IgGs and >100-fold better IC_{50} than the parental Fabs (Fig.1g).

126   CoV-X2 remained effective against pseudoviruses bearing escape mutations that made them

127   resistant to the individual mAbs (Fig.1g)[15] and against a pseudovirus with RBD mutations found

128   in the B.1.351 variant (first reported in South Africa, IC_{50} =1.3 nM (191 ng/mL); Extended data

129   Fig. 5). To confirm CoV-X2 efficacy, we performed plaque reduction neutralization assays with

130   infectious virus. CoV-X2 efficiently neutralized: SARS-CoV-2 (IC_{50} = 0.9 nM); the D614G variant

131   first appearing in Europe (B.1, IC_{50} = 0.2 nM); the B.1.1.7 variant first observed in the United

132   Kingdom (IC_{50} = 0.2 nM); the B.1.1.248 variant first isolated in Brazil (IC_{50} = 2.1 nM) and B.1.351

133   first isolated in South Africa (IC_{50} = 12 nM; Fig.1h). The latter two have almost identical mutations

134   in the RBD, the only difference being N vs. T at position 417, which does not interact with

135   CoV-X2. Nonetheless, neutralization of B.1.351 was lower, suggesting either some

136   conformational differences in the RBD or long-range effects deriving from other mutations in the

137   S protein. A similar behavior is seen with the wild-type sequence (D614), which has lower

138   neutralization than G614 even if no other difference is present; a plausible explanation is that G614

139   makes the CoV-X2 epitopes more accessible by favoring the RBD 'up' conformation.[17] We

140   conclude that the *in vitro* binding and neutralizing properties of CoV-X2 make it preferable over

141   its parental antibodies.

142   To assess the clinical potential of CoV-X2, we investigated its ability to protect animals

143   from infection and disease. We first developed a novel mouse model in which human ACE2

144   (hACE2) is expressed by upper and lower respiratory tract cells upon inhalation of a modified

145   Adeno Associated Virus (AAV-hACE2, see Methods, Fig.2 and Extended Data Fig.7).

Fig.2 | CoV-X2 protects AAV-hACE2-transduced mice against SARS-CoV-2 disease. a, Loss of body weight over time in SARS-CoV-2 infected mice. 13 to 15 weeks old C57Bl/6NCrl wild-type female mice were transduced with AAV-hACE2 by forced inhalation, which provides delivery of viral particles to both upper and lower respiratory tract. After >7 days, mice were either infected with SARS-CoV-2 (1×10^4 pfu) or received vehiculum by the intranasal route. Weight was monitored daily for 8 days (SARS-CoV-2, n = 5; control, n = 4). Mean with standard deviation is shown. **b,** Kinetic of viral burden in the lungs from

153 SARS-CoV-2-infected mice by plaque assays. Mean with standard deviation; the dashed line indicates the
154 limit of detection. **c,** Kinetic of viral RNA levels in lung samples from SARS-CoV-2-infected mice by RT-
155 qPCR. Mean with standard deviation. **d,** Schematic of the experimental layout. Wild-type mice were
156 transduced with AAV-hACE2 by forced inhalation. After >7 days, mice were inoculated intraperitoneally
157 (i.p) with 150 µg of antibodies. One day later, the mice were infected intranasally (i.n.) with SARS-CoV-2
158 (1x10^4 pfu). **e,** Changes in body weight upon infection were monitored daily in antibody-treated mice
159 (C121, n=9; C135, n=5; CoV-X2, n=13; isotype control, n=10). Mean with standard deviation is shown. **f,**
160 Lung viral burden by plaque assay at 5 dpi (isotype control, n=6; CoV-X2, n=10). The dashed line indicates
161 the limit of detection; mean with standard deviation. P value was calculated with two-tailed Student's t test.
162 **g,** Spleen viral RNA levels by RT-qPCR at 5 and 8 dpi (gray: isotype control; purple: CoV-X2). Mean with
163 standard deviation. P value was calculated with two-tailed Student's t test. **h,** Photographs of lungs collected
164 from infected mice (8 dpi). **i,** Histopathology and F4/80 immunohistochemistry (IHC). Hematoxylin and
165 Eosin-stained (H&E) sections of paraffin-embedded lungs from infected mice (8 dpi). Arrowheads point to
166 foamy macrophages. F4/80 IHC shows abundant macrophage infiltration in lungs of mice treated with
167 isotype control but not with CoV-X2.

168

169 This approach enables rapid production of large cohorts of animals and has the advantage of being

170 applicable to wild-type and mutant mouse colonies, independently of age and gender. Moreover,

171 since AAV vectors are only weakly immunogenic and cytotoxic, the system allows for prolonged

172 expression of hACE2[18-21] (Extended Data Fig.7). SARS-CoV-2 infection of ACE2 humanized

173 mice results in progressive weight loss, respiratory pathology and disease requiring culling on day

174 8 post infection (dpi, Fig.2a–c and Extended Data Fig.7).

175 To evaluate the protective effect of antibodies, hACE2 mice were treated with antibody

176 (150 µg) one day before SARS-CoV-2 challenge and monitored over time (Fig.2d–i). Upon

177 intranasal infection with 1x10^4 pfu of SARS-CoV-2 (SARS-CoV-2/human/Czech

178 Republic/951/2020), isotype control treated animals showed weight loss starting at 3 dpi, and by

179 8 dpi most animals had lost approximately 25–30% of their body weight reaching humane endpoint

180 (Fig.2e). Infectious virus could be recovered from the lungs (Fig.2f), viral RNA was detected also

181 in the spleen (Fig.2g) but not in the heart (data not shown). Lung pathology resembled severe

182 COVID-19 in humans[22] and was characterized by Diffuse Alveolar Damage (DAD; 50-80% of

183 tissue area), alveolar replacement with infiltrates of immune cells and fibroblasts, thickened septa

184   and infiltrations by activated macrophages with foamy cytoplasm (Fig.2i). In contrast, animals

185   treated with CoV-X2 maintained their body weight (P<0.0001 at 4–8 dpi when compared to

186   isotype; Fig.2e; P values between all groups in Extended Data Table1), had reduced viral RNA in

187   the spleen (Fig.2g) and displayed neither macro- nor histopathological changes (DAD <5-10%,

188   Fig.2h,i). While infectious virus could be readily recovered from controls (5 of 6), it was only

189   recovered from 1 out of 10 CoV-X2 treated animals at 5 dpi (Fig. 2f) and could not be recovered

190   from any of 13 animals at 8 dpi (data not shown). Since none of the CoV-X2 treated mice exhibited

191   symptoms at any time, we conclude that CoV-X2 protects mice from infection and disease.

192   Since monotherapy with C121 or C135 mAbs leads to virus escape *in vitro*[15], we treated

193   hACE2 mice with the individual antibodies and sequenced the virus. Only wild-type RBD

194   sequences were obtained from controls (n=10). Instead, the virus in mice treated with C121

195   selected for a mutation resulting in E484D (5 of 5 mice that were analyzed at 8 dpi). C121 escape

196   mutations at E484 were previously observed *in vitro*[15] and changes at this residue (present also in

197   the B.1.351 and B.1.1.248 variants) reduce neutralization by human sera by more than 10-fold[23].

198   E484D affects intermolecular H-bonds at the core of the C121/RBD interface and it is suggested

199   to increase the RBD affinity for ACE2[24]. Virus with D484 is pathogenic, since 7 out of 9 mice

200   treated with C121 developed disease (Fig.2e) and only D484 virus was found in their lungs. In

201   contrast, and unlike the *in vitro* results[15], no virus evasion or pathology was observed in mice

202   treated with C135 (n=5; Fig.2e and data not shown). In CoV-X2 treated animals, even though no

203   infectious virus was retrieved (8 dpi, n=13) and no symptoms ever noticed, low levels of residual

204   viral RNA could be detected in some animals after 40 cycles of PCR amplification: in 6 of 13

205   animals the virus sequence was wild-type and in 2 mice overlapping sequencing traces were

206   consistent with coexistence of wild-type and D484. Thus, in those 2 of 13 animals with D484 CoV-

207   X2 remained protective even if the mutation diluted the effective antibody concentration,

208   presumably leaving only the C135 moiety active. Finally, CoV-X2 was protective also when

209   administered 12 hours after SARS-CoV-2 challenge (Extended Data Fig.8)

210   Monoclonal antibodies targeting the SARS-CoV-2 S are in advanced clinical trials and

211   show promise against COVID-19[1,2]. Concomitant use of multiple antibodies is preferred for

212   increased efficacy and added resistance against viral evasion. Indeed, the virus can escape pressure

213   by a single antibody *in vitro* and, as shown here, also in animals. Moreover, RBD mutations

214   threatening the efficacy of single monoclonals have already been detected in virus circulating in

215   minks and humans[25], including mutations at the C121 and C135 epitopes (Extended Data Fig.9).

216   One disadvantage of antibody cocktails is the requirement for twice or more the development and

217   production capacity than for single mAbs, which is a significant challenge in light of the

218   augmented demand due to COVID-19 related vaccines and therapeutics on top of the need to

219   maintain production of biologics for other diseases.[4]

220   Multispecific antibodies offer the advantages of cocktails in a single molecule. Indeed, we

221   have shown that the CoV-X2 bispecific is more effective than the related monoclonals at inhibiting

222   ACE2 binding; it has sub-nanomolar IC_{50} against a broader array of viral sequences; and it protects

223   animals from SARS-CoV-2 even when C121, its potent parental mAb, fails due to the insurgence

224   of viral escape. C135, the other parental mAb, did not generate escape in our animal experiment

225   but readily generated them *in vitro*[15]. CoV-X2 is expected to be more resistant to viral escape

226   compared to monoclonals. Indeed, we have shown that CoV-X2 binds and neutralizes mutants not

227   recognized by its parental mAbs as well as variants of concern that recently emerged in United

228   Kingdom[13], South Africa[14] and Brazil[26].

229   CoV-X2, unlike other multispecifics[27], is a fully human IgG-like molecule. As such, it has

230   favorable developability and could be further engineered to alter effector functions. For example,

231   the Fragment crystallizable (Fc) of CoV-X2 was already modified to modulate its interaction with

232   Fc receptors and complement (LALA-PG mutations)[28] without affecting its antigen-binding

233   properties. The LALA modification prevents Antibody Dependent Enhancement (ADE) of

234   flavivirus infection[29,30] and it may be a desirable modification also in the context of SARS-CoV-

235   2, since cellular and animal experiments with coronaviruses, including SARS-CoV[31-33], support

236   the possibility of ADE. Other modifications, like LS[28] for increased half-life, are easily achievable.

237   Finally, CoV-X2 is human-derived and produced in a format (CrossMab) already shown to be safe

238   in clinical trials[34], which further supports its developability. Thus, IgG-like bispecifics are worth

239   adding to the arsenal employed to combat SARS-CoV-2 and its plausible future mutations.

240

241   **References:**

242   1   DeFrancesco, L. COVID-19 antibodies on trial. *Nat Biotechnol* **38**, 1242-1252,
243   doi:10.1038/s41587-020-0732-8 (2020).
244   2   Klasse, P. J. & Moore, J. P. Antibodies to SARS-CoV-2 and their potential for
245   therapeutic passive immunization. *Elife* **9**, doi:10.7554/eLife.57877 (2020).
246   3   Robbiani, D. F. *et al.* Convergent antibody responses to SARS-CoV-2 in convalescent
247   individuals. *Nature* **584**, 437-442, doi:10.1038/s41586-020-2456-9 (2020).
248   4   Dawn M. Ecker & Seymour, P. Supply and Demand Trends: Mammalian
249   Biomanufacturing Industry Overview. *CPhInsights* (2020).
250   5   Baum, A. *et al.* REGN-COV2 antibodies prevent and treat SARS-CoV-2 infection in
251   rhesus macaques and hamsters. *Science* **370**, 1110-1115, doi:10.1126/science.abe2402
252   (2020).
253   6   Schäfer, A. *et al.* Antibody potency, effector function, and combinations in protection
254   and therapy for SARS-CoV-2 infection in vivo. *Journal of Experimental Medicine* **218**,
255   doi:10.1084/jem.20201993 (2020).
256   7   Schlake, T. *et al.* mRNA: A Novel Avenue to Antibody Therapy? *Mol Ther* **27**, 773-784,
257   doi:10.1016/j.ymthe.2019.03.002 (2019).
258   8   Tiwari, P. M. *et al.* Engineered mRNA-expressed antibodies prevent respiratory syncytial
259   virus infection. *Nature communications* **9**, 3999, doi:10.1038/s41467-018-06508-3
260   (2018).

261   9   Rybakova, Y. *et al.* mRNA Delivery for Therapeutic Anti-HER2 Antibody Expression
262   In Vivo. *Mol Ther* **27**, 1415-1423, doi:10.1016/j.ymthe.2019.05.012 (2019).
263   10   Barnes, C. O. *et al.* SARS-CoV-2 neutralizing antibody structures inform therapeutic
264   strategies. *Nature*, doi:10.1038/s41586-020-2852-1 (2020).
265   11   Schaefer, W. *et al.* Immunoglobulin domain crossover as a generic approach for the
266   production of bispecific IgG antibodies. *Proc Natl Acad Sci U S A* **108**, 11187-11192,
267   doi:10.1073/pnas.1019002108 (2011).
268   12   Walls, A. C. *et al.* Structure, Function, and Antigenicity of the SARS-CoV-2 Spike
269   Glycoprotein. *Cell* **181**, 281-292.e286, doi:10.1016/j.cell.2020.02.058 (2020).
270   13   Kemp, S. *et al.* Recurrent emergence and transmission of a SARS-CoV-2 Spike deletion
271   ΔH69/V70. *bioRxiv*, 2020.2012.2014.422555, doi:10.1101/2020.12.14.422555 (2020).
272   14   Tegally, H. *et al.* Emergence and rapid spread of a new severe acute respiratory
273   syndrome-related coronavirus 2 (SARS-CoV-2) lineage with multiple spike mutations in
274   South Africa. *medRxiv*, 2020.2012.2021.20248640, doi:10.1101/2020.12.21.20248640
275   (2020).
276   15   Weisblum, Y. *et al.* Escape from neutralizing antibodies by SARS-CoV-2 spike protein
277   variants. *eLife* **9**, e61312, doi:10.7554/eLife.61312 (2020).
278   16   Schmidt, F. *et al.* Measuring SARS-CoV-2 neutralizing antibody activity using
279   pseudotyped and chimeric viruses. *J Exp Med* **217**, doi:10.1084/jem.20201181 (2020).
280   17   Benton, D. J. *et al.* The effect of the D614G substitution on the structure of the spike
281   glycoprotein of SARS-CoV-2. *Proceedings of the National Academy of Sciences* **118**,
282   e2022586118, doi:10.1073/pnas.2022586118 (2021).
283   18   Han, K. *et al.* Lung Expression of Human ACE2 Sensitizes the Mouse to SARS-CoV-2
284   Infection. *Am J Respir Cell Mol Biol*, doi:10.1165/rcmb.2020-0354OC (2020).
285   19   Hassan, A. O. *et al.* A SARS-CoV-2 Infection Model in Mice Demonstrates Protection
286   by Neutralizing Antibodies. *Cell* **182**, 744-753.e744, doi:10.1016/j.cell.2020.06.011
287   (2020).
288   20   Sun, J. *et al.* Generation of a Broadly Useful Model for COVID-19 Pathogenesis,
289   Vaccination, and Treatment. *Cell* **182**, 734-743.e735, doi:10.1016/j.cell.2020.06.010
290   (2020).
291   21   Sun, S. H. *et al.* A Mouse Model of SARS-CoV-2 Infection and Pathogenesis. *Cell Host*
292   *Microbe* **28**, 124-133.e124, doi:10.1016/j.chom.2020.05.020 (2020).
293   22   Deshmukh, V., Motwani, R., Kumar, A., Kumari, C. & Raza, K. Histopathological
294   observations in COVID-19: a systematic review. *Journal of clinical pathology*, jclinpath-
295   2020-206995, doi:10.1136/jclinpath-2020-206995 (2020).
296   23   Greaney, A. J. *et al.* Comprehensive mapping of mutations to the SARS-CoV-2 receptor-
297   binding domain that affect recognition by polyclonal human serum antibodies. *bioRxiv*,
298   2020.2012.2031.425021, doi:10.1101/2020.12.31.425021 (2021).
299   24   Chen, J., Wang, R., Wang, M. & Wei, G. W. Mutations Strengthened SARS-CoV-2
300   Infectivity. *J Mol Biol* **432**, 5212-5226, doi:10.1016/j.jmb.2020.07.009 (2020).
301   25   Weisblum, Y. *et al.* Escape from neutralizing antibodies by SARS-CoV-2 spike protein
302   variants. *Elife* **9**, doi:10.7554/eLife.61312 (2020).
303   26   Hoffmann, M. *et al.* SARS-CoV-2 variants B.1.351 and B.1.1.248: Escape from
304   therapeutic antibodies and antibodies induced by infection and vaccination. *bioRxiv*,
305   2021.2002.2011.430787, doi:10.1101/2021.02.11.430787 (2021).

306   27   Dong, J. *et al.* Development of humanized tri-specific nanobodies with potent
307   neutralization for SARS-CoV-2. *Scientific reports* **10**, 17806, doi:10.1038/s41598-020-
308   74761-y (2020).
309   28   Saunders, K. O. Conceptual Approaches to Modulating Antibody Effector Functions and
310   Circulation Half-Life. *Frontiers in immunology* **10**, 1296,
311   doi:10.3389/fimmu.2019.01296 (2019).
312   29   Dejnirattisai, W. *et al.* Cross-reacting antibodies enhance dengue virus infection in
313   humans. *Science* **328**, 745-748, doi:328/5979/745 [pii]
314   10.1126/science.1185181 (2010).
315   30   Sridhar, S. *et al.* Effect of Dengue Serostatus on Dengue Vaccine Safety and Efficacy. *N*
316   *Engl J Med* **379**, 327-340, doi:10.1056/NEJMoa1800820 (2018).
317   31   Yip, M. S. *et al.* Antibody-dependent infection of human macrophages by severe acute
318   respiratory syndrome coronavirus. *Virol J* **11**, 82, doi:10.1186/1743-422x-11-82 (2014).
319   32   Jaume, M. *et al.* Anti-severe acute respiratory syndrome coronavirus spike antibodies
320   trigger infection of human immune cells via a pH- and cysteine protease-independent
321   FcγR pathway. *J Virol* **85**, 10582-10597, doi:10.1128/jvi.00671-11 (2011).
322   33   Yip, M. S. *et al.* Antibody-dependent enhancement of SARS coronavirus infection and its
323   role in the pathogenesis of SARS. *Hong Kong Med J* **22**, 25-31 (2016).
324   34   Klein, C. *et al.* Engineering therapeutic bispecific antibodies using CrossMab technology.
325   *Methods* **154**, 21-31, doi:10.1016/j.ymeth.2018.11.008 (2019).
326

Author contributions

R.D.G, M.Pe., L.S., F.Mu., J.C.L., F.Ma, D.M., C.I., E.P., S.D.G., M.Pa., F.B., D.M., S.Gi., C.O.B, F.B., J.C.S, F.G, S.Ga, designed and carried out experiments and analyzed results, produced plasmids, antibodies and viral proteins. P.N., T.M., J.H., V.H, B.M., N.P., A.F., J.T., V.I., M.Pa., D.Z., P.B., I.B., P.S., D.R., performed animal experiments and analyzed the results. L.V, D.F.R., D.R., Q.P.H., A.P., L.C., P.J.B., M.C.N., P.D.B., T.H. conceived and designed study and

351   experiments and analyzed the results. P.N., T.M., R.N., O.P., J.P., J.R., R.S. conceived and

352   designed the mouse model. L.V., D.F.R., D.R, R.D.G. wrote the manuscript with input from all

353   co-authors.

354   **Competing interests**

355   In connection with this work the Institute for Research in Biomedicine has filed a provisional

356   patent application on which L.V. is inventor (PCT/EP2020/085342). The Rockefeller University

357   has filed a provisional patent application on coronavirus antibodies on which D.F.R. and M.C.N.

358   are inventors.

359

360   **Extended data figures**
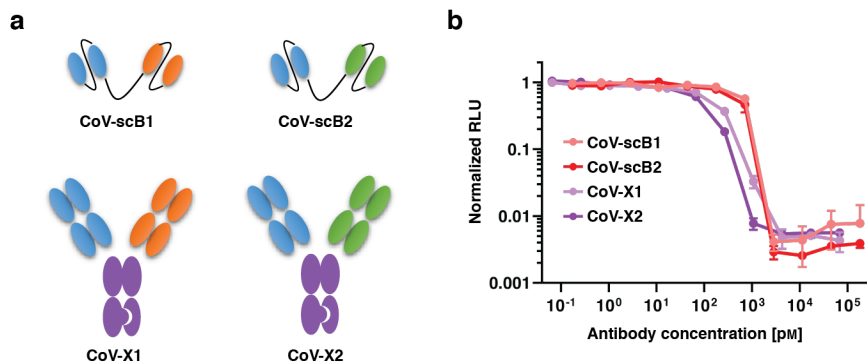
361
362   **Extended Data Fig.1 | Neutralization of SARS-CoV-2 pseudovirus by bispecific antibodies. a,**
363   Schematic representation of the 4 bispecific constructs; two in scFv format and two as IgG-like CrossMAb
364   with knob-in-hole. The parental monoclonals forming the bispecifics are color-coded (C135 blue, C144
365   orange, C121 green; Fc region in purple). **b,** All 4 constructs neutralize SARS-CoV-2 pseudovirus *in vitro*
366   at sub-nanomolar concentrations (IC$_{50}$: 0.13, 0.04, 0.74 and 0.53 nM for CoV-X1, CoV-X2, CoV-scB1 and
367   CoV-scB2, respectively). Normalized relative luminescence values, which correlate to infection, are
368   reported versus antibody concentration, as detailed in Schmidt *et al.*[16]. Mean with standard deviation is
369   shown, representative of two independent experiments.
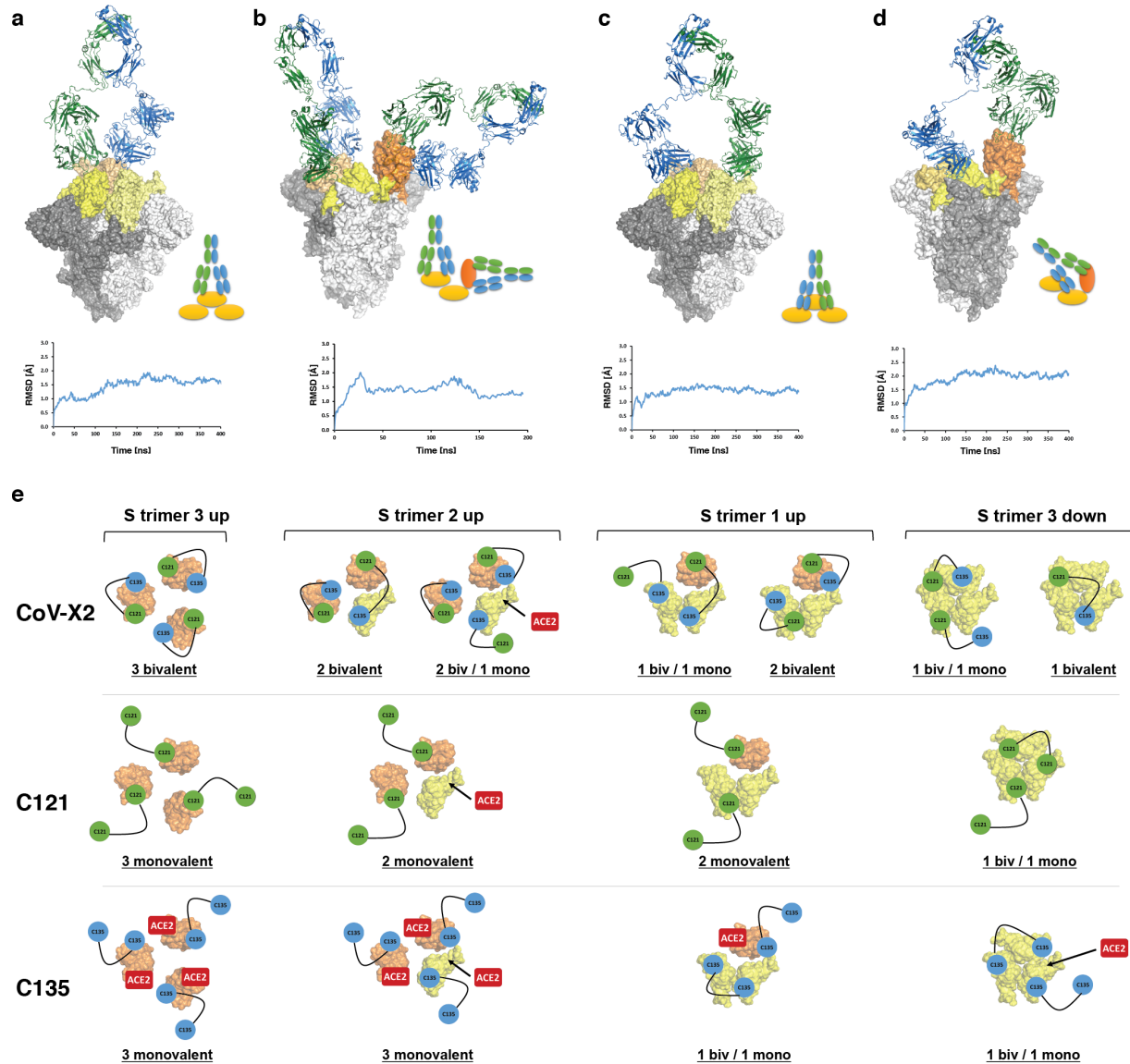
Extended Data Fig.2 | CoV-X2 engages its epitopes on all RBD conformations on the S trimer. a–d, Molecular Dynamics (MD) simulations of the complex between the CoV-X2 bispecific and S trimers with RBD in either all down, all up or mixed up/down conformations show that CoV-X2 can engage a single RBD with both arms (**a,b**), two adjacent RBDs in the down conformation (**c**), and two RBDs in the up/down conformation (**b,d**). The complexes were subjected to up to 400 ns of fully atomistic MD simulations to assess feasibility and stability of the bound conformations. Root-mean-squared deviations (RMSD) values are shown to indicate structural stability. S trimer is in shades of grey, RBDs in yellow (down conformation) and orange (up), the C121 and C135 moieties of CoV-X2 are in green and blue, respectively. **e,** Schematic representation of the computationally predicted binding modes of CoV-X2, C121 IgG and C135 IgG on the S trimer, colored as in **a–d**. Antibodies are represented by connected circles; ACE2 is in red on the RBD if it can bind directly to a given conformation; it has an arrow pointing to the RBD if ACE2 binding is achieved after an allowed switch to the up conformation. For example, in the 3-up conformation (left), CoV-X2 can engage all the RBDs with bivalent binding, whereas C121 and C135 can only achieve monovalent binding. C135 binding does not prevent interaction with ACE2. The situation is similar in the

16

385 other S conformations (2-up 1-down, 2-down 1-up and 3-down), with only the bispecific achieving bivalent

386 interaction and preventing ACE2 access in all conformations.
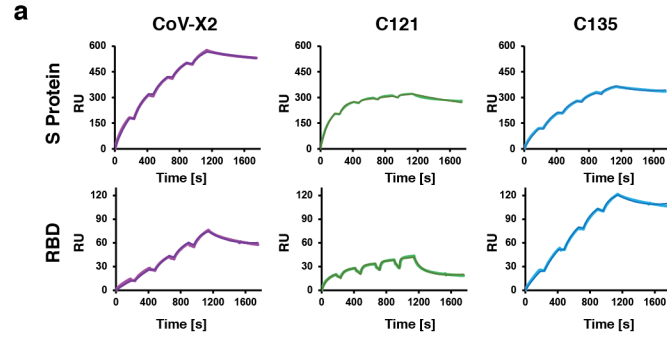
			CoV-X2	C121	C135
Spike protein	k_a [$\cdot 10^6$ M^{-1}s^{-1}]		0.69	1.33	0.62
	k_d [$\cdot 10^{-3}$s^{-1}]		0.12	0.17	0.13
	K_D [nM]		0.18	0.13	0.21
RBD	k_a [$\cdot 10^6$ M^{-1}s^{-1}]		0.58	1.30	0.20
	k_d [$\cdot 10^{-3}$s^{-1}]		1.35	3.15	0.12
	K_D [nM]		2.35	2.40	0.59

387

388 **Extended Data Fig.3 | CoV-X2 and its parental mAbs bind recombinant, isolated RBD and S trimer**
389 **with low nanomolar affinity. a,** Representative SPR traces from which the data in (**b**) was derived. **b,**
390 Kinetic parameters for the binding of C121 IgG, C135 IgG, and CoV-X2 to S trimer and RBD.

a

	CoV-X2 K_D [nM]	C121 K_D [nM]	C135 K_D [nM]
Wild-type	2.3	2.4	0.6
N331A	2.1	0.3	0.4
E340K	1.4	1.9	<0.1
T345A	1.2	1.4	0.2
V367F	2.4	2.1	0.5
R408I	1.9	2.1	0.7
K417A	1.3	0.7	0.3
W436R	2.7	3.3	2.7
K444E	1.1	2.8	No binding
E484A/F486A	7.8	No binding	1.7
F490A	2.9	35	1.5
T500A	1.5	1.5	1.0
Y505A	1.4	1.6	0.6
R346T/A372T/I402V/ K417R/Q498H/H519K (Pangolin GD)	2.5	0.5	No binding
D614G	3.2	0.6	1.6

b
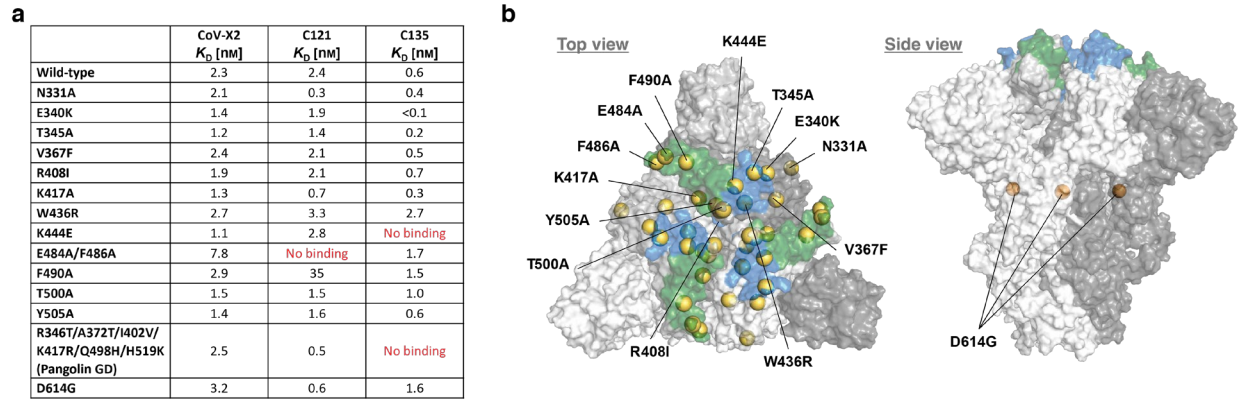
Extended Data Fig.4 | CoV-X2 binds with low-nanomolar affinity to S protein mutants, including some that are not recognized by the parental mAbs C121 and C135. a, SPR-derived binding affinities of CoV-X2, C121 IgG and C135 IgG to several S trimer mutants. **b,** Mutations tested in (**a**) are indicated by yellow spheres on the surface representation of the S trimer. The epitopes of C121 (green) and C135 (blue) are shown.

397
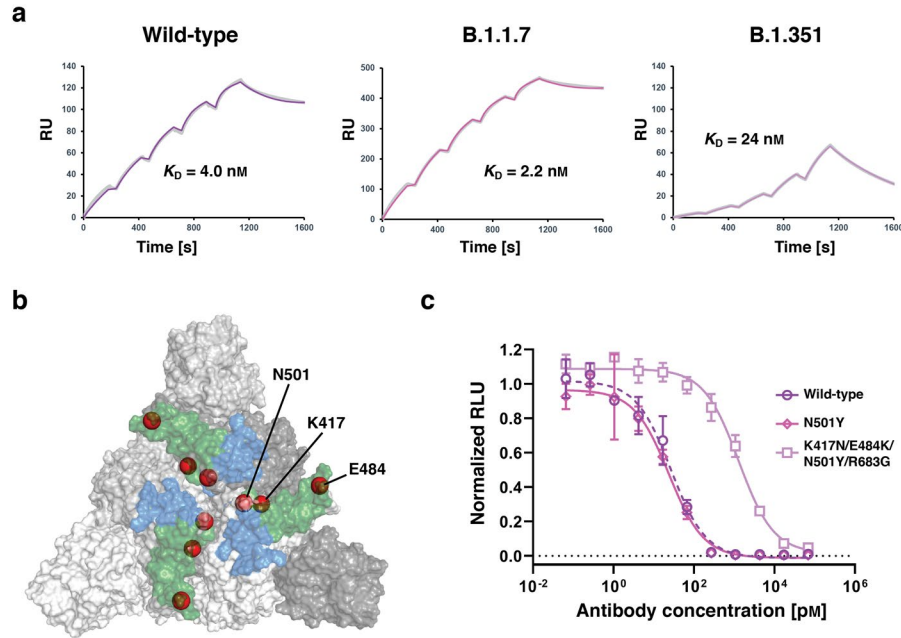
Extended Data Fig.5 | Efficacy of CoV-X2 against B.1.1.7 and B.1.351 variants. a, SPR traces showing binding of CoV-X2 to the RBD corresponding to wild-type, B.1.1.7 (also known as UK) and B.1.351 (also known as South African) variants of SARS-CoV-2. **b,** Residues mutated in the variants are shown as red spheres on the surface representation of the S trimer. The epitopes of C121 (green) and C135 (blue) are shown. **c,** Neutralization of SARS-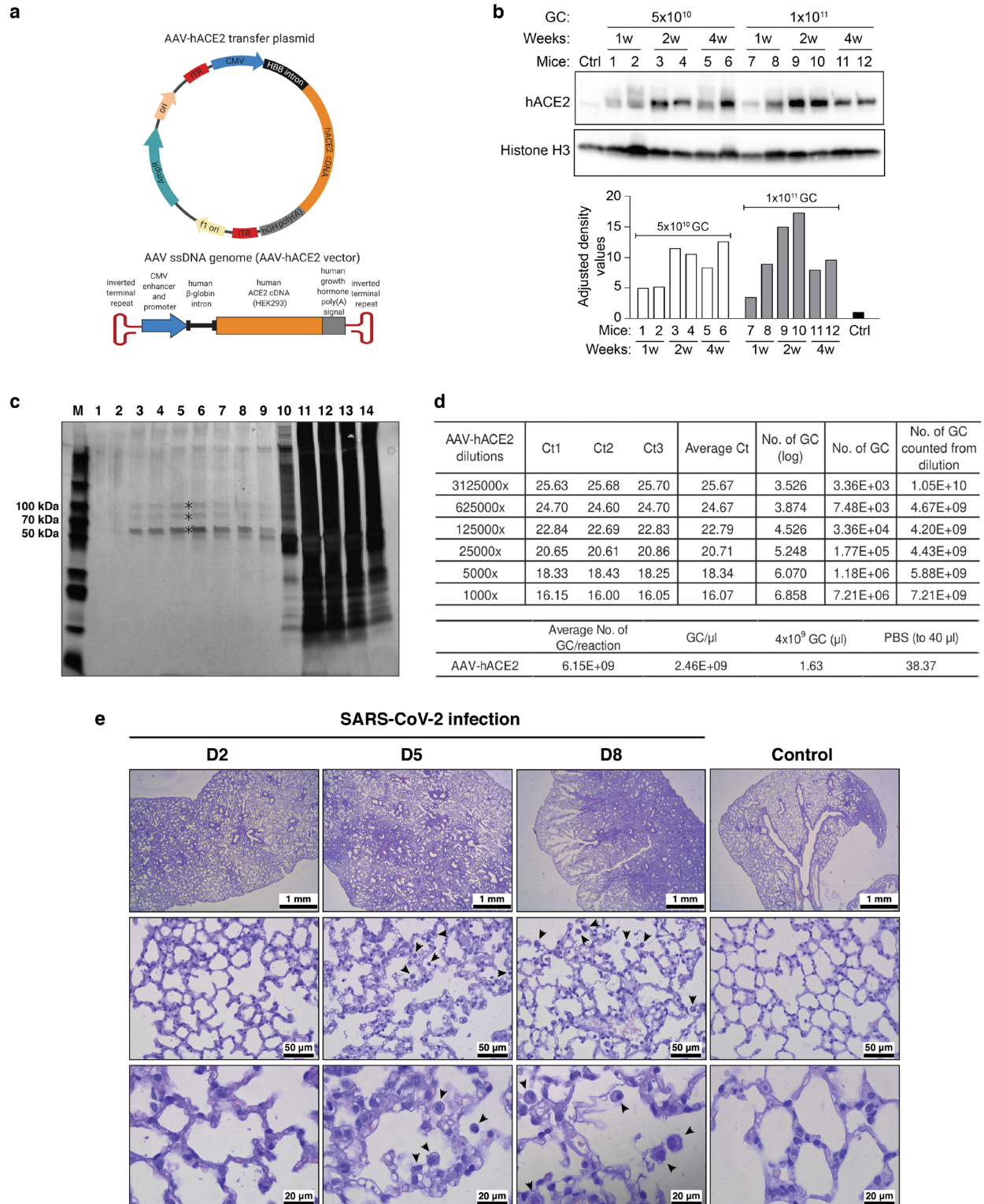CoV-2 pseudoviruses expressing wild-type, N501Y and K417N/E484K/N501Y/R683G (corresponding to South African mutants in the RBD, see Figure 1h) S protein by CoV-X2.

405

a

c

	Immobilized on the chip				
	RBD 150 nM	RBD 75 nM	RBD 15 nM	RBD 5 nM	
C135 Fab	1.0	1.2	1.7	1.7	k_a Normalized $k_a(X_i\,nM)/k_a(150\,nM)$
C135 IgG	1.0	1.1	1.0	0.9	
C121 IgG	1.0	1.1	3.1	2.6	
CoV-X2	1.0	1.4	1.8	2.0	
C135 Fab	1.0	1.1	1.0	0.9	k_d Normalized $k_d(X_i\,nM)/k_d(150\,nM)$
C135 IgG	1.0	2.3	9.1	18.8	
C121 IgG	1.0	3.2	9.0	18.5	
CoV-X2	1.0	1.3	3.2	5.7	

b
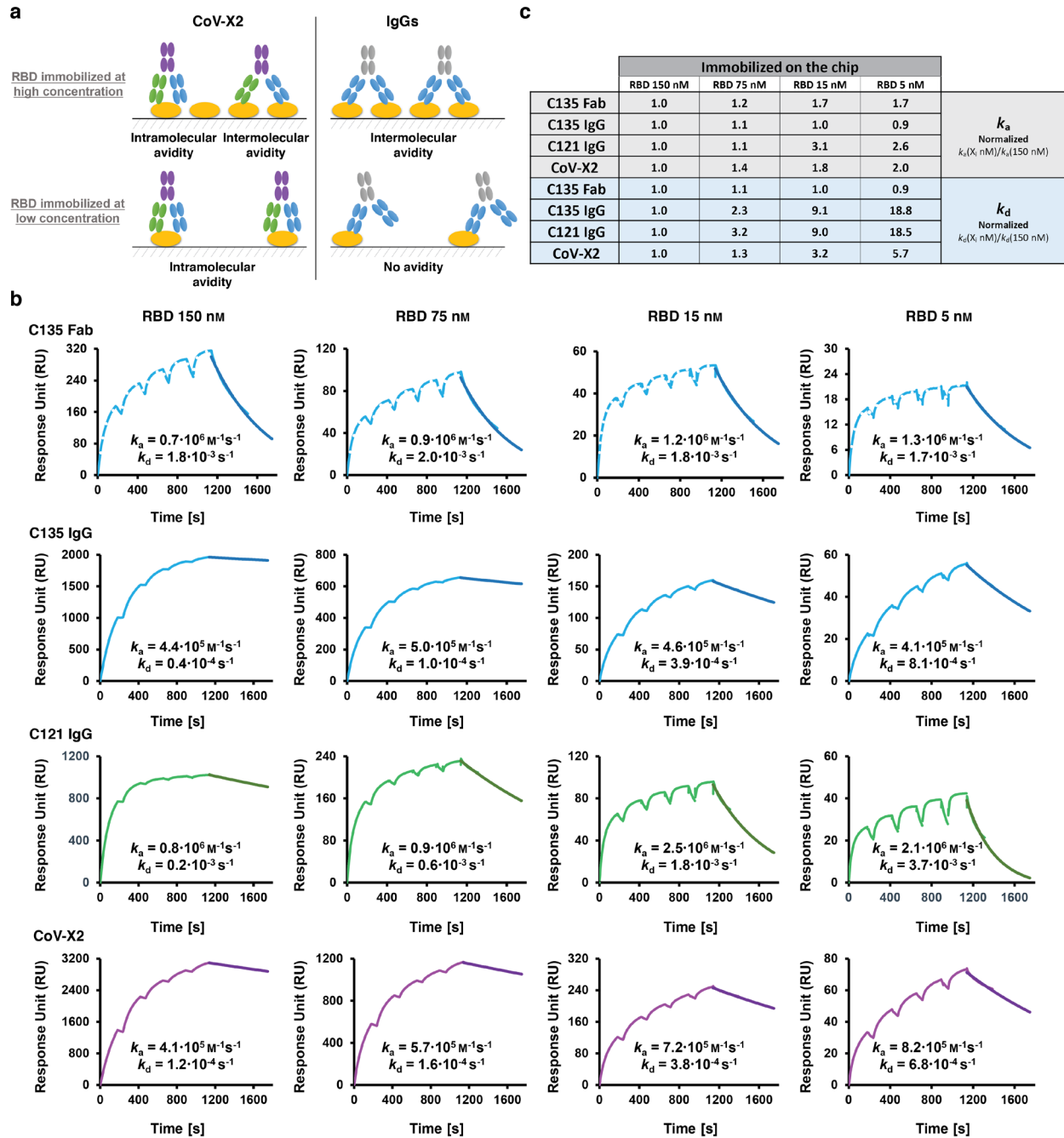
406
407 **Extended Data Fig.6 | SPR-based avidity assays confirm that CoV-X2 can engage bivalently on a**
408 **single RBD. a,** CoV-X2 and monoclonal IgGs (C121 or C135) have different binding modes available
409 when high or low quantities of RBD are immobilized on the surface of the SPR chip. mAbs have avidity
410 effects at high RBD concentrations due to intermolecular binding, which results in slower dissociation rate
411 (k_d), but not at low RBD concentrations, since bivalent binding to a single RBD is impossible. In contrast,
412 the bispecific has avidity at both high and low concentrations, since bivalent binding to its two epitopes on
413 a single RBD is possible. k_a is not affected by avidity. **b,** Experimental confirmation that CoV-X2 engages
414 bivalently on a single RBD. SPR traces used to determine k_a and k_d of mAbs, Fab and bispecific at different
415 concentrations of immobilized RBD (see Fig.1d) are shown. **c,** Table summarizing the SPR results plotted
416 in Fig.1d. k_a and k_d were normalized against the values at the highest RBD concentration. k_a and Fab k_d were

417   unaffected by the RBD concentration, as expected. k_d became faster for the monoclonals (loss of avidity)
418   but less so for the bispecific (avidity maintained due to simultaneous binding to two sites on a single RBD).

d

AAV-hACE2 dilutions	Ct1	Ct2	Ct3	Average Ct	No. of GC (log)	No. of GC	No. of GC counted from dilution
3125000x	25.63	25.68	25.70	25.67	3.526	3.36E+03	1.05E+10
625000x	24.70	24.60	24.70	24.67	3.874	7.48E+03	4.67E+09
125000x	22.84	22.69	22.83	22.79	4.526	3.36E+04	4.20E+09
25000x	20.65	20.61	20.86	20.71	5.248	1.77E+05	4.43E+09
5000x	18.33	18.43	18.25	18.34	6.070	1.18E+06	5.88E+09
1000x	16.15	16.00	16.05	16.07	6.858	7.21E+06	7.21E+09

	Average No. of GC/reaction	GC/μl	4×10^9 GC (μl)	PBS (to 40 μl)
AAV-hACE2	6.15E+09	2.46E+09	1.63	38.37

e

419
420 **Extended Data Fig.7 | Generation of the new AAV-hACE2-transduced mouse model for COVID-19.**
421 **a,** Diagram of the AAV-hACE2 plasmid and corresponding Adeno Associated viral vector. **b,** Western blot
422 analysis detecting hACE2 expression in the lungs of one non-transduced control mouse (Ctrl) and 12 mice
423 transduced with two different doses of AAV-hACE2 viral particles (5×10^{10} or 1×10^{11} genome copies (GC)).
424 Lung tissue was collected 1, 2, or 4 weeks (w) post transduction. Histone H3 was used as control for

425 quantification (bottom). **c,** Preparation of concentrated AAV-hACE2. AAV-hACE2 plasmid was co-
426 transfected with pHelper and AAV Rep/Cap 2/9n vectors into 293AAV cells (see Methods). In order to
427 increase viral titers, viral particles from both cell lysate and PEG-precipitated growth medium were
428 ultracentrifuged in discontinuous iodixanol gradient. The silver-stained SDS-PAGE gel shows 14
429 consecutive fractions: 1-9 represent enriched AAV fractions used for experiments, whereas fractions 10–
430 14 are contaminated with proteinaceous cell debris. Iodixanol was chosen as a density gradient medium
431 due to its low toxicity *in vivo* and its easy removal by ultrafiltration. M is protein marker, * are AAV capsid
432 proteins VP1, VP2, and VP3. **d,** The amount of AAV particles was estimated by qRT-PCR. The number of
433 genome copies (GC) expressed as log was calculated from a standard curve. From one 15 cm^2 dish, 75 µl
434 with $2.0x10^{12}$ GC/ml were prepared, which is sufficient for hACE2 humanization of 37 mice. **e,** Kinetic of
435 lung histopathology in SARS-CoV-2 infected ACE2 humanized mice. Hematoxylin and Eosin-stained
436 sections showed inflammatory infiltrates composed of lymphocytes, macrophages, neutrophils, and
437 fibroblasts replacing the alveoli. The size of the affected areas increased over time (area of diffuse alveolar
438 damage: control <5-10%, 2 dpi <10-30%, 5 dpi 20-80 %, 8 dpi 50-90%). Alveolar septa were thickened in
439 areas close to infiltrates. In samples collected at 5 and 8 dpi, an increased number of activated macrophages
440 with foamy cytoplasm (black arrowheads) was seen. AAV-hACE2 transduced, SARS-CoV-2 uninfected
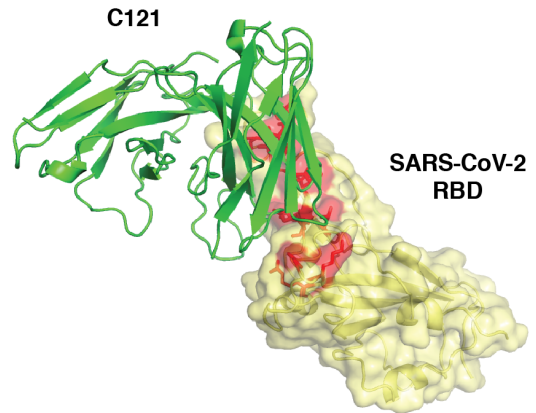441 mice were used as control and showed no significant pathology.
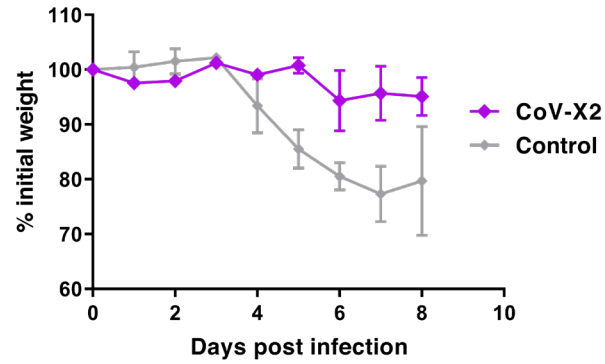
442
443 **Extended Data Fig.8 | Post-exposure administration of CoV-X2 protects SARS-CoV-2 infected mice**
444 **from disease.** Animals were infected intranasally with 10^4 pfu of SARS-CoV-2 and treated with
445 250 µg/mouse of either isotype control antibody (n=3) or CoV-X2 (n=2) 12 hours later. Weight loss and
446 pathological signs were apparent in control but not in CoV-X2 treated animals.
447

a

wt	mutant	Strain Name	wt	mutant	Strain Name
Arg403	Lys	/USA/VA-DCLS-0630/2020 /USA/VA-DCLS-0439/2020 /AUS/VIC1787/2020	Gly485	Arg	/AUS/VIC1829/2020 /AUS/VIC1960/2020 /AUS/VIC1693/2020 /AUS/VIC1660/2020 /AUS/VIC1683/2020 /AUS/VIC1588/2020 /AUS/VIC1565/2020 /AUS/VIC1611/2020 /AUS/VIC1812/2020 /AUS/VIC2023/2020
Lys444	Asn	/AUS/VIC4515/2020			
Gly446	Asp	/USA/FL-BPHL-2211/2020			
Gly446	Val	/USA/MN-MDH-1430/2020 /AUS/VIC913/2020 /AUS/VIC6087/2020 /AUS/VIC9542/2020	Cys488	Arg	/IRN/COVID19-IRVSH4/2020
Leu452	Gln	/USA/VA-DCLS-1404/2020	Phe490	Leu	/AUS/VIC10024/2020 /AUS/VIC766/2020
Leu452	Arg	/USA/CA-CZB-12872/2020	Phe490	Val	/USA/MA-MGH-01415/2020
Leu452	Met	/BHR/340798279_S5_L001/2020 /USA/CA-CZB-1043/2020 /IND/906/2020	Pro491	His	/IND/906/2020
Leu455	Phe	/AUS/VIC10121/2020 /AUS/VIC5196/2020	Gln493	Leu	/USA/WI-UW-371/2020
Val483	Ala	/USA/WA-UW-6527/2020 /USA/WA-UW-1587/2020 /USA/WA-RML-2/2020 /USA/WA-RML-6/2020 /USA/WA-RML-5/2020 /USA/UT-03764/2020	Ser494	Pro	/USA/CA-CZB-4047/2020 /USA/CA-CZB-11677/2020 /USA/CA-CZB-6994/2020 /USA/CA-CZB-11010/2020 /USA/MI-MDHHS-SC20047/2020 /USA/CA-CZB-12810/2020 /USA/VIC9505/2020
Val483	Phe	/AUS/VIC2139/2020 /USA/MA-UW-629/2020	Ser494	Leu	/AUS/VIC5057/2020
Glu484	Gln	/USA/UT-UPHL-2009538/2020 /IND/GBRC278a/2020 /USA/SEARCH-1462-SAN/2020			
Glu484	Lys	/USA/UT-QDX-1869/2020 /BHR/340859913_S11/2020 /USA/IL-UW-379/2020			
Glu484	Ala	/USA/VA-DCLS-1615/2020			

b

wt	mutant	Strain Name
Phe342	Leu	England/01, 1/29
Ala344	Ser	/USA/WA-S2278/2020 /USA/WA-S2530/2020
Ala344	Thr	/IND/GBRC431a/2020
Ala344	Val	/AUS/VIC10958/2020
Thr345	Ser	/USA/WA-S1049/2020
Thr345	Ile	/PER/covper051/2020
Arg346	Thr	/IND/GBRC333/2020
Trp436	Thr	/IND/GBRC333/2020
Asn439	Lys	/USA/IL-UW/799/2020
Asn440	Lys	/HKG/Case5138/2020
Leu441	Ile	/USA/FL-BPHL-0297/2020
Asn450	Lys	/IND/906/2020
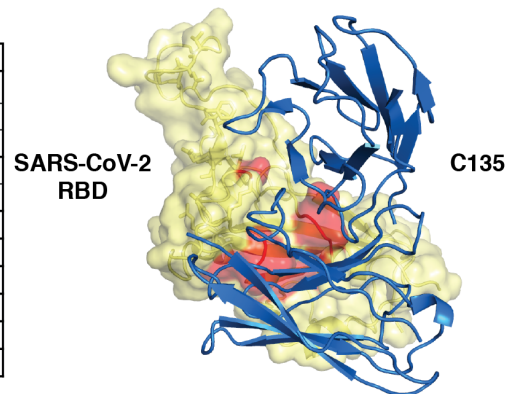
448

449 **Extended Data Fig.9 | Natural SARS-CoV-2 variants in the C121 and C135 epitopes.** Summary of
450 naturally occurring mutations in the C121 (**a**) or C135 (**b**) epitopes reported in circulating SARS-CoV-2
451 (as of January 1, 2021). The location of the mutated residues is shown in red on the RBD structure. C121
452 and C135 variable regions are in green and blue (PDB ID: 7K8X and 7K8Z respectively).
453

	C121	C135	CoV-X2	Isotype control
C121	–	P<0.0001	P<0.0001	P<0.01
C135	P<0.0001	—	P>0.05	P<0.0001
CoV-X2	P<0.0001	P>0.05	—	P<0.0001
Isotype control	P<0.01	P<0.0001	P<0.0001	—

Extended Data Table 1 | Summary of the P values for the mouse protection experiment. Statistical comparison of body weight differences in animals treated with the individual monoclonal antibodies (C121 or C135), the CoV-X2 bispecific or isotype control at 8 dpi (related to Fig. 2e). P values were determined with the ANOVA test. Comparison of the entire curves (Fig. 2e) by the One Sample Wilcoxon Test or by the ANOVA followed by Turkey-Kramer post-test reveals that the isotype control treated group is statistically different from any of the other groups (CoV-X2, C135, or C121; P<0.05).